Acta Cryst. (1993). A**49**, 436-445

Transmission Low-Energy Electron Diffraction (TLEED) and its Application to the Low-Voltage Point-Projection Microscope

BY W. QIAN, J. C. H. SPENCE AND J. M. ZUO

Department of Physics, Arizona State University, Tempe, AZ 85287, *USA*

(*Received* 20 *March* 1992; *accepted* 8 *October* 1992)

Abstract

Solutions to the mixed Bragg-Laue case for transmission low-energy electron diffraction (TLEED) are derived for thin crystalline slabs and applied to the low-voltage (0-1 kV) field-emission point-projection transmission microscope [Fink, Schmid, Kreuzer & Wierbicki (1991). *Phys. Rev. Lett.* **67**, 1543-1546]. Absorption due to inelastic scattering, exchange and virtual inelastic scattering effects are considered. The relationship between Fourier imaging, shadow imaging, holography of extended objects and holography of small objects is briefly discussed, together with the optimum energy for atomic-resolution electron microscopy and holography. The importance of multiple scattering in transmission-electron interference patterns obtained at LEED energies with spherical-wave illumination is evaluated and the nature of the optical potential that might be recovered holographically is discussed.

1. Introduction

This paper describes transmission low-energy electron diffraction (TLEED) calculations for electrons in the 100-1000 eV range incident on thin crystalline metal films a few atomic layers thick. The many-beam Bloch-wave method has been used to treat this mixed Bragg-Laue case and back-reflected LEED beams are also included. The results of the computations are applied to the interpretation of the point-projection electron images recently reported by Fink, Schmid, Kreuzer & Wierzbicki (1991) to determine the importance of multiple scattering for the interpretation of these images. We also study the conditions of voltage and specimen thickness for which a holographic interpretation may be given to the results and for which the required reference beam exists.We are concerned in this paper mainly with periodic scattering objects whose dimensions are infinite (or much larger than the electron probe) in directions normal to the electron beam. The case of small objects bathed within the beam, for which rays passing around the object may act as a holographic reference wave, are briefly discussed in the light of our results in § 5.

The point-projection electron microscope was first developed by Boersch (1942) and Gabor's proposal for in-line point-source holography was first attempted using this geometry by Haine & Mulvey (1952). Lack of source brightness and incoherent instabilities rendered this early effort at electron holography largely unsuccessful. Modern work has used field-emission guns in the off-axis geometry [see Tonomura (1987) for a review]. Recently, however, striking new results have been obtained at LEED energies without using lenses in the in-line geometry (Fink *et al.*, 1991).

Since the penetration of electrons at LEED energies ($10 < V < 1000$ eV) is a few nm, for a sufficiently thin crystal just a few atomic layers thick, appreciable intensity may be transmitted through it to form an image. Fig. 1(*a*) shows the geometry of our variant of the field-emission point-projection electron microscope (Fink *et al.*, 1991). If the angular range (measured at the sample) over which the electron beam is coherent exceeds the Bragg angle and if the sample is periodic, a Fourier image (Cowley & Moodie, 1960) forms on a distant screen. This is an unaberrated image of the periodic component of the wavefield $\Psi(1)$ shown across the exit face of the crystal. This image is formed without lenses or scanning on certain downstream planes with magnification $M \simeq z_2/z_1$, where z_2 and z_1 are defined in Fig. 1(*a*). Experimental Fourier images of this type with $z_1 \simeq 200$ nm and $z_2 \simeq 10$ cm have recently been reported at an electron energy of about 300 V, showing apparent atomic resolution (Fink *et al.*, 1991). Fourier images are formed by interference between rays leaving the tip at angles differing by multiples of the Bragg angle, which interfere after diffraction on passing through the crystal. In an earlier paper (Spence & Qian, 1992), we showed that lensless Fourier imaging is possible in the presence of strong multiple scattering, calculated the images to be expected and discussed the factors limiting ultimate resolution. Here we are chiefly concerned with the scattering processes inside the crystal rather than with Fourier-imaging theory. However, in § 5, we discuss briefly the relationship between Fourier imaging, shadow imaging, point-projection electron holography and multiple scattering.

The dynamical theory of electron diffraction in the reflection geometry was first introduced by Bethe (1928) and adapted to the transmission geometry by

0108-7673/93/030436-10$06.00

Blackman (1939). A modern formulation, appropriate to the RHEED geometry, was given by Collela (1972). Reviews are given by Metherell (1975) and Humphreys (1979). Although these theories were developed for transmission high-energy electron diffraction (THEED) in the 10 keV–1 MeV range, they may readily be extended to LEED energies (provided that convergence is fully tested) and are then well suited to our problem. [Other computational schemes for LEED and RHEED also exist and might also be used (Pendry, 1974; Zhao & Tong, 1988; Maksym, 1988).] An illuminating discussion of the relationship between band theory for low-energy crystal electrons and the dynamical theory of electron diffraction was given by Stern, Perry & Boudreaux (1969). This uses a Bloch-wave treatment for electrons with moderate energies (100–1000 eV) and includes both forward- and backscattered beams.

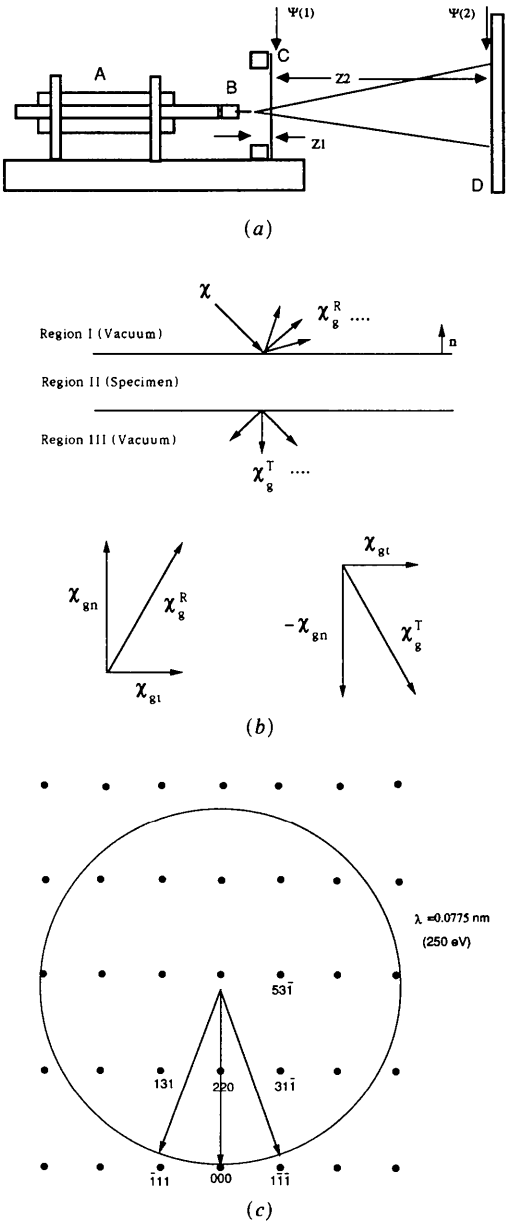

Fig. 1. (*a*) Geometry of the point-source projection microscope. *A*: Inchworm positioning device. *B*: STM tube scanner, with tip at high negative potential. *C*: Thin semitransparent ground crystal of thickness *t*. *D*: Microchannel-plate detector. Image wavefunction $\Psi(1)$ and detector wavefunction $\Psi(2)$ are shown. (*b*) Schematic drawing of the electron wave vectors in three regions. The crystal normal $\mathbf{n}$ is also shown. The sample is assumed to have uniform thickness *t*. Two wave vectors χ_{gn}, χ_{gt} and their relationship to χ_g^T and χ_g^R are also shown. (*c*) The Ewald sphere drawn to scale for these calculations. The electron energy is 250 eV and the wavelength is 0.775 Å.

The simplifying approximations of THEED theory, which may fail at low energies, must be considered. For energies of 100–1000 eV, the electron wavelength is in the range 1–0.3 Å so that the diameter of the Ewald sphere is comparable with the reciprocal-lattice spacing. The two-beam extinction distance is about 1 nm and small-angle scattering approximations cannot always be made. The Bragg angle θ_B may be greater than 10° and strong absorption occurs. Unlike the THEED case, it is important to include backscattered beams to account for all multiple-scattering processes. The absorption coefficients used to describe the depletion of the elastic wavefield by inelastic scattering must be investigated, since the coefficients used for high-energy electrons (Bird & King, 1990) may not be applicable. Exchange and virtual inelastic scattering effects cannot be ignored, as in THEED, and their corrections to the crystal potential must be estimated.

In this paper, we present a general formalism for many-beam dynamical diffraction for transmission low-energy electron diffraction, using the Bloch-wave method. 'Absorption' resulting from inelastic scattering has been included through the use of a complex optical potential and an estimate of this given. Corrections to the crystal potential due to exchange effects between the incident and crystal electrons have been included using the local-density approximation. The effect of virtual inelastic scattering on the real part of the crystal potential is discussed. Example calculations corresponding to the experimental conditions used by Fink *et al.* (1991) for thin gold films are presented and discussed.

2. Theory

2.1. *The dispersion equations. Backscattering*

The wavefield incident on the crystal in the experiments of Fink *et al.* (1991) is approximately a spherical wave with a divergence greater than twice the Bragg angle. This results in coherent overlapping diffraction orders, which necessarily produce Fourier images (Cowley, 1981). In this paper, we are interested in the multiple-scattering aspects of the problem and so consider illumination by a plane wave. The

complete image for a periodic parallel-sided slab-shaped crystal may then be synthesized from a sum of incident plane waves differing in angle by multiples of the Bragg angle or by using the theorem of reciprocity. [For a ray diagram showing how Fourier imaging results from coherent overlapping diffraction orders and virtual sources, see Spence & Qian (1992)]. Following Bethe's original formulation (Bethe, 1928), the total electron wavefield within the crystal excited by an incident plane wave $\exp(2\pi i\boldsymbol{\chi}\cdot\mathbf{r})$ can be written as a linear combination of Bloch waves

$$\Psi(\mathbf{r})=\sum_j \mathbf{b}^{(j)}\psi^{(j)}(\mathbf{r}) \tag{1}$$

with $\psi^{(j)}(\mathbf{r})$, the Bloch wave in state j, given by

$$\psi^{(j)}(\mathbf{r})=\sum_{\mathbf{g}} C_{\mathbf{g}}^{(j)}\exp[2\pi i(\mathbf{k}^{(j)}+\mathbf{g})\cdot\mathbf{r}]. \tag{2}$$

All Bloch waves correspond to the same total energy. The Bloch-wave excitation coefficients $b^{(j)}$ are determined by the boundary conditions, whereas the wave amplitudes $C_{\mathbf{g}}^{(j)}$ and the wave vectors $k^{(j)}$ for each Bloch wave are obtained by solving the time-independent Schrödinger equation

$$\nabla^2\psi(\mathbf{r})+(8\pi^2 me/h^2)[V(\mathbf{r})+E]\psi(\mathbf{r})=0, \tag{3}$$

where m is the relativistically corrected electron mass, h is Planck's constant, eE is the total electron energy and $V(\mathbf{r})$ is the periodic crystal potential, which can be expanded in the form of a Fourier series

$$V(\mathbf{r})=\sum_{g}(h^2/2me)U_g\exp(2\pi i\mathbf{g}\cdot\mathbf{r}). \tag{4}$$

Here, the potential $V(\mathbf{r})$ and its Fourier coefficients $V_{\mathbf{g}}$ are positive, while the potential energy $eV(\mathbf{r})$ is negative. Substitution of (2) and (4) into (3) yields a set of equations for the wave amplitudes (Hirsch, Howie, Nicholson, Pashley & Whelan, 1977).

$$[\mathbf{K}^2-(\mathbf{k}^{(j)}+\mathbf{g})^2]C_{\mathbf{g}}^{(j)}+\sum_{\mathbf{h}\neq\mathbf{0}} U_{\mathbf{h}}C_{\mathbf{g}-\mathbf{h}}^{(j)}=0, \tag{5}$$

where

$$K=[(2meE/h^2)+U_0]^{1/2}=(\chi^2+U_0)^{1/2} \tag{6}$$

is the amplitude of the electron wave vector within the crystal after correction by the mean inner potential U_0. $\boldsymbol{\chi}$ is the incident electron wave vector in vacuum.

The crystal slab is assumed to be parallel sided and infinite in directions normal to the beam. Matching of the wavefield outside the crystal with that excited inside at the entrance surface requires equality of the tangential components,

$$\mathbf{k}_t^j=\boldsymbol{\chi}_t=\mathbf{K}_t. \tag{7}$$

We now let

$$\mathbf{k}^j=\mathbf{K}+\gamma^{(j)}\mathbf{n}, \tag{8}$$

where $\mathbf{n}$ is a unit vector in the outward surface-normal direction and the *Anpassung* γ is given by

$$\gamma^{(j)}=k_n^j-K_n. \tag{9}$$

Substituting (8) into (5), we obtain a set of equations with $\gamma^{(j)}$ and $C_{\mathbf{g}}^{(j)}$ as the only unknowns,

$$[\mathbf{K}^2-(\mathbf{K}+\mathbf{g})^2-2(\mathbf{K}+\mathbf{g})\cdot\mathbf{n}\gamma^{(j)}-\gamma^{(j)^2}]C_{\mathbf{g}}^{(j)}+\sum_{\mathbf{h}\neq\mathbf{0}} U_{\mathbf{h}}C_{\mathbf{g}-\mathbf{h}}^{(j)}=0. \tag{10}$$

This can be further simplified as

$$(-\gamma^{(j)^2}+\alpha_{\mathbf{g}}\gamma^{(j)}-\beta_{\mathbf{g}})C_{\mathbf{g}}^{(j)}+\sum_{\mathbf{h}\neq\mathbf{0}} U_{\mathbf{h}}C_{\mathbf{g}-\mathbf{h}}^{(j)}=0, \tag{11}$$

where

$$\alpha_{\mathbf{g}}=-2(\mathbf{K}_z-\mathbf{g}_z), \tag{12}$$

$$\beta_{\mathbf{g}}=\mathbf{g}^2+2\mathbf{g}\cdot\mathbf{K}. \tag{13}$$

Equation (11) can be converted into an eigenvalue equation by defining a column vector $\{C_{\mathbf{g}}^{(j)}\}$ whose elements are the amplitudes $C_{\mathbf{g}}^{(j)}$

$$(-\gamma^{(j)^2}\mathbf{I}+\gamma^{(j)}\mathbf{B}-\mathbf{D})\{C_{\mathbf{g}}^{(j)}\}=0. \tag{14}$$

Here, $\mathbf{I}$ is a unit matrix and $\mathbf{B}_{\mathbf{gh}}=0$, $\mathbf{B}_{\mathbf{gg}}=\alpha_{\mathbf{g}}$; $\mathbf{D}_{\mathbf{gh}}=-\mathbf{U}_{\mathbf{gh}}$; $\mathbf{D}_{\mathbf{gg}}=\beta_{\mathbf{g}}$. In general, (14) yields $2n$ eigenvalues $\gamma^{(j)}$ and, therefore, $2n$ eigenvectors $\{C_{\mathbf{g}}^{(j)}\}$. There are thus $2n$ plane-wave components within the crystal with wave vectors $\mathbf{k}^{(j)}$. Of these, n represent waves traveling in the forward direction, while the other n represent waves traveling backwards. Thus, (14) includes all of the backscattered and forward-scattered waves within the crystal.

To simplify the eigenvalue equation, we define a new vector $\{X_{\mathbf{g}}^{(j)}\}$ such that (Kambe, 1988)

$$(\gamma^{(j)}\mathbf{I}-\mathbf{B})\{C_{\mathbf{g}}^{(j)}\}=\{X_{\mathbf{g}}^{(j)}\} \tag{15}$$

and then (14) becomes

$$\gamma^{(j)}\{X_{\mathbf{g}}^{(j)}\}=\mathbf{0}\{X_{\mathbf{g}}^{(j)}\}-\mathbf{D}\{C_{\mathbf{g}}^{(j)}\}. \tag{16}$$

Here $\mathbf{0}$ is a null matrix. Combining (15) and (16), we obtain a new eigenvalue equation with $2n$ components,

$$\mathbf{A}\{Y_{\mathbf{g}}^{(j)}\}=\gamma^{(j)}\{Y_{\mathbf{g}}^{(j)}\}, \tag{17}$$

where (Collela, 1972)

$$\{Y_{\mathbf{g}}^{(j)}\}=\begin{Bmatrix} C_{\mathbf{g}}^{(j)} \\ X_g^{(j)} \end{Bmatrix} \tag{18}$$

is a column vector of $2n$ components and

$$\mathbf{A}=\begin{bmatrix} \mathbf{B} & \mathbf{I} \\ -\mathbf{D} & \mathbf{0} \end{bmatrix}$$

is a $2n\times 2n$ supermatrix. Equation (17) can be readily solved by numerical methods provided that the structure factors $U_{\mathbf{g}}$ are all known.

2.2. *Boundary conditions. The mixed Bragg–Laue case in TLEED*

As shown in Fig. 1(*b*), an incident plane wave impinging on the entrance surface of a crystal slab results in n beams backreflected into vacuum region I and $2n$ Bloch waves excited within the crystal in region II. Of these, there are n beams forward scattered beyond the exit surface at $z=-t$ into the vacuum in region III. Since the Bloch-wave formalism considers the total wavefield within the crystal, the waves backscattered by the second interface together with all of the multiple-scattering effects are included in the solutions of the eigenvalue equation (17). Thus, the total wavefield in each region can be expressed as

$$\Psi_{\rm I}(\mathbf{r}) = \exp(2\pi i\boldsymbol{\chi}\cdot\mathbf{r}) + \sum_{\mathbf{g}} R_{\mathbf{g}} \exp(2\pi i\boldsymbol{\chi}_{\mathbf{g}}^{R}\cdot\mathbf{r}),$$

$$\Psi_{\rm II}(\mathbf{r}) = \sum_{j=1}^{2n} \mathbf{b}^{(j)} \sum_{\mathbf{g}} C_{\mathbf{g}}^{(j)} \exp[2\pi i(\mathbf{k}^{(j)}+\mathbf{g})\cdot\mathbf{r}], \quad (19)$$

$$\Psi_{\rm III}(\mathbf{r}) = \sum_{\mathbf{g}} T_{\mathbf{g}} \exp(2\pi i\boldsymbol{\chi}_{\mathbf{g}}^{T}\cdot\mathbf{r}),$$

where $R_{\mathbf{g}}$ and $T_{\mathbf{g}}$ are the reflection and transmission coefficients, respectively. The wave vectors in the vacuum $\boldsymbol{\chi}_{\mathbf{g}}^{R}$ and $\boldsymbol{\chi}_{\mathbf{g}}^{T}$ can be determined by applying the energy-conservation condition for elastic scattering. Hence, if inelastic scattering is neglected,

$$|\boldsymbol{\chi}| = |\boldsymbol{\chi}_{\mathbf{g}}^{R}| = |\boldsymbol{\chi}_{\mathbf{g}}^{T}|. \quad (20)$$

To match each plane-wave component of $\Psi(\mathbf{r})$ at both vacuum–crystal interfaces, the tangential components of the wave vectors must be equal,

$$\boldsymbol{\chi}_{\mathbf{g}t}^{R} = \boldsymbol{\chi}_{\mathbf{g}t}^{T} = \mathbf{k}_t^{j} + \mathbf{g}_t. \quad (21)$$

Equations (20) and (21) determine the vacuum wave vectors $\boldsymbol{\chi}_{\mathbf{g}}^{R}$ and $\boldsymbol{\chi}_{\mathbf{g}}^{T}$. We define two wave vectors $\boldsymbol{\chi}_{\mathbf{g}t}$ and $\boldsymbol{\chi}_{\mathbf{g}n}$ in the tangential and normal directions such that

$$\boldsymbol{\chi}_{\mathbf{g}t} = \boldsymbol{\chi}_t + \mathbf{g}_t,$$
$$\boldsymbol{\chi}_{\mathbf{g}n} = [\chi^2 - (\boldsymbol{\chi}_t + \mathbf{g}_t)^2]^{1/2}\mathbf{n}.$$

The total electron wave function (19) can then be written

$$\begin{aligned}\Psi_{\rm I}(\mathbf{r}) &= \exp(2\pi i\boldsymbol{\chi}\cdot\mathbf{r}) \\ &\quad + \sum_{\mathbf{g}} R_{\mathbf{g}} \exp[2\pi i(\boldsymbol{\chi}_{\mathbf{g}t}+\boldsymbol{\chi}_{\mathbf{g}n})\cdot\mathbf{r}], \\ \Psi_{\rm II}(\mathbf{r}) &= \sum_{j=1}^{2n} b^{(j)} \sum_{\mathbf{g}} C_{\mathbf{g}}^{(j)} \exp[2\pi i(\mathbf{K}+\gamma^{(j)}\mathbf{n}+\mathbf{g})\cdot\mathbf{r}], \\ \Psi_{\rm III}(\mathbf{r}) &= \sum_{\mathbf{g}} T_{\mathbf{g}} \exp[2\pi i(\boldsymbol{\chi}_{\mathbf{g}t}-\boldsymbol{\chi}_{\mathbf{g}n})\cdot\mathbf{r}].\end{aligned} \quad (22)$$

Imposing boundary conditions for the total electron wave function on both surfaces, we obtain

$$\begin{aligned}\delta_{\mathbf{g}0} + R_{\mathbf{g}} &= \sum_{j=1}^{2n} b^{(j)} C_{\mathbf{g}}^{(j)}, \\ \chi_n\delta_{\mathbf{g}0} + \chi_{\mathbf{g}n}R_{\mathbf{g}} &= \sum_{j=1}^{2n} b^{(j)} C_{\mathbf{g}}^{(j)}(K_n+\gamma^{(j)}+g_n), \\ T_{\mathbf{g}} \exp(2\pi i\chi_{\mathbf{g}n}t) &= \sum_{j=1}^{2n} b^{(j)} C_{\mathbf{g}}^{(j)} \exp[-2\pi i(K_n+\gamma^{(j)}+g_n)t], \\ \chi_{\mathbf{g}n}T_{\mathbf{g}} \exp(2\pi i\chi_{\mathbf{g}n}t) &= -\sum_{j=1}^{2n} b^{(j)} C_{g}^{(j)}(K_n+\gamma^{(j)}+g_n) \\ &\quad \times \exp[-2\pi i(K_n+\gamma^{(j)}+g_n)t].\end{aligned} \quad (23)$$

This set of $4n$ equations contains $4n$ unknowns. Thus, $T_{\mathbf{g}}$, $R_{\mathbf{g}}$ and $b^{(j)}$ are readily solved by standard numerical methods.

3. Corrections to the crystal potential

For real crystals, the incident electron beam undergoes elastic scattering, refraction and inelastic scattering. In addition, for low-energy electrons (10–1000 eV), exchange effects between the incident and crystal electrons and virtual inelastic scattering effects need to be considered. As for the case of keV electrons (Hirsch *et al.*, 1977; Yoshioka 1957), these effects can be accounted for by suitable corrections to the crystal potential. We assume that (as for gold) the crystal contains a center of symmetry. Then the total effective 'optical' potential seen by the incident electrons can be written as

$$V_{\rm eff}(\mathbf{r}) = V(\mathbf{r}) + V_{\rm ex}(\mathbf{r}) + \Delta V(\mathbf{r}) + iV'(\mathbf{r}), \quad (24)$$

where $V(\mathbf{r})$ is the positive elastic part of the potential [the potential energy $eV(\mathbf{r})$ is negative], $V_{\rm ex}(\mathbf{r})$ is the exchange potential, $\Delta V(\mathbf{r})$ is the real contribution to the crystal potential due to virtual inelastic scattering and $iV'(\mathbf{r})$ is the imaginary part of the potential, which takes account of depletion of the elastic wavefield by inelastic processes ('absorption'). These modifications to the crystal potential mean that the $2n\times 2n$ supermatrix $\mathbf{A}$ is no longer Hermitian and the eigenvalues $\gamma^{(j)}$ become complex. The Hartree electrostatic part of the potential $V(\mathbf{r})$ was obtained from a superposition of spherical neutral atoms by use of the Mott–Bethe relationship (Humphreys, 1979) between X-ray and electron structure factors and the X-ray scattering factors tabulated in *International Tables for Crystallography* (1992). These are based on relativistic Hartree–Fock calculations for isolated atoms.

3.1. *Exchange corrections*

The exchange poential $V_{\rm ex}(\mathbf{r})$ results from the antisymmetric nature of the total electron wavefunction

Table 1. *Fourier components of the optical potential used (in* V)

$$V_{\rm eff}(\mathbf{r}) = V(\mathbf{r}) + V_{\rm ex}(\mathbf{r}) + \Delta V(\mathbf{r}) + iV'(\mathbf{r}).$$

g	$V_{\rm eff}(\mathbf{g})$ Total	$V(\mathbf{g})$ Elastic	$V_{\rm ex}(\mathbf{g})$	$\Delta V(\mathbf{g})$	$V'(\mathbf{g})$ Total
000	$39.3+5.7i$	28.4	8.0	2.9	5.7
002	$16.9+1.7i$	16.9	~0.0	0	1.7
111	$19.7+1.9i$	18.8	~0.0	0	1.9
2-20	$12.3+1.2i$	12.3	~0.0	0	1.2

under the exchange of electrons–in this case the beam and crystal electrons. This repulsion between electrons of like spin makes a positive contribution to $V_{\rm eff}(\mathbf{r})$, making the potential energy $eV_{\rm eff}(\mathbf{r})$ more negative (Slater, 1951). For THEED, this correction has been shown to be negligible (Rez, 1978) since the high-energy beam electron is distinguishable from the lower-energy crystal electrons, but the correction becomes appreciable at low energies. The accurate determination of the exchange energy requires a full solution of the Hartree–Fock equations using self-consistent methods. However, various approximations have been made for LEED (Pendry, 1974). The expressions given by Slater (1967), based on the local approximation, is commonly used in LEED and we adopt it here, taking

$$V_{\rm ex}(\mathbf{r}) = \alpha V_{\rm Slater}(\mathbf{r}), \tag{25}$$

where $V_{\rm Slater}(\mathbf{r})$ is given (in SI units) by

$$V_{\rm Slater}(\mathbf{r}) = C\rho^{1/3}(\mathbf{r})$$

with

$$C = 3(e/4\pi\varepsilon_o)(3/8\pi)^{1/3}$$

and $\alpha \simeq \frac{1}{3}$ for most materials, where $\rho(\mathbf{r})$ is the local electron density in units of number of electrons per unit volume. Calculations based on this agree well with LEED experimental data at energies up to about 200 eV (Pendry, 1974).

This correction may be included by adding an additional term to the structure factor $U_{\rm g}$, where, from (4),

$$U_{\rm g}^{\rm ex} = (2me/h^2)\, V_{\rm ex}(\mathbf{g}), \tag{26}$$

where $V_{\rm ex}(\mathbf{g})$ is a Fourier coefficient of the exchange potential $V_{\rm ex}(\mathbf{r})$. The local three-dimensional electron density was generated for our calculations using X-ray atomic scattering factors taken from the *International Tables for Crystallography* (1992) and the rigid-ion approximation. The results for $V_{\rm ex}(\mathbf{g})$ are listed in Table 1.

3.2. *Inelastic scattering. 'Absorption'*

In addition to elastic Bragg scattering, the beam electron may excite all the accessible elementary excitation of the crystal during its traversal. These inelastic scattering processes cause an attenuation of the electric wavefield, while the (later) decay of the excitations generates various secondary-emission products. Energy deposited in the sample may be dissipated as heat (phonons) or result in ionization of atoms, leading ultimately to radiation damage *via* the radiolysis mechanism. At the low energies considered here, direct displacement of atoms by ballistic collisions cannot occur. We are not interested here in the decay products of inelastic scattering (which may cause damage) but in the effect of inelastic scattering on the attenuation of the elastic Bragg beams. The inelastic scattering mechanisms can be distinguished as localized or delocalized. Plasmon excitations in the valence band of metals (with energy of the order of 10–20 eV) form a major source of inelastic scattering. Since this is delocalized, it contributes only to the mean absorption V_0', causing an equal exponential attenuation of all beams with thickness. An estimate of V_0' for LEED has been made by Lundqvist (1969) based on perturbation theory and Feynman-diagram analysis. From this theoretical estimate and from experimental measurements by LEED, it has been concluded (Pendry, 1974) that, for most materials, $V_0' \simeq 4$ eV within a factor of two at a beam energy of 100 eV.

The second major contribution to absorption is thermal diffuse scattering, consisting of phonon excitations with energies 0.1–0.01 eV. This scattering is localized within the crystal unit cell and so causes 'anomalous' absorption of LEED beams. Several calculations of the Fourier coefficients $V_{\rm g}'$ of the contribution to the absorption potential $V'(\mathbf{r})$ describing excitation of phonons at different temperatures have been published for THEED (Bird & King, 1990; Radi, 1970). These are based on the original formulation of Hall & Hirsch (1965), which adopts an Einstein model for lattice vibrations. Calculations based on this model for low energies E produce unrealistic results ($V_{\rm g}' > V_{\rm g}$) owing to the use of plane waves for the final scattering state rather than Bloch waves. Experimental results for anomalous absorption in LEED are scarce; however, Jones McKinney & Webb (1966) find for Ag at room temperature the empirical result

$$\mu_{\rm g} = 1.4E^{-1/2}\ \text{Å}^{-1} \tag{27}$$

if E is in V and μ is the intensity absorption coefficient. This expression gives $V_{\rm g}'({\rm phonon})/V_{\rm g} \simeq 0.1$ and was used in our calculations, as shown in Table 1.

The excitation of inner-shell atomic electrons is also an important inelastic scattering process for high-energy electrons. For low-energy beam electrons, this effect is small (or absent) for the inner localized excitations, since the ionization thresholds involved are comparable with or greater than the beam energy. For the outer shells (*e.g.* the valence band in semiconductors), the excitations are more delocalized and the

main effect is a small increase in the mean absorption. Since the value used for V_0' is matched to experimental data, we have lumped this contribution together with the plasmon contribution V_0'.

3.3. *Virtual inelastic scattering*

Inelastic scattering events that are forbidden by classical kinematics but allowable within the time–energy uncertainty principle are known as virtual events. The first attempt to estimate the effects of virtual inelastic scattering for THEED was given by Yoshioka (1957). Based on this original expression, Rez (1978) pointed out that phonon scattering does not contribute to this potential because phonon energies are too small. Plasmon scattering also gives no contribution to the Fourier coefficients V_g ($\mathbf{g} \neq \mathbf{0}$) of the virtual inelastic scattering potential because plasmon scattering is delocalized. The only contribution comes from single-electron excitations, particularly the excitation of localized inner-shell electrons. Rez's calculations for 100 kV electrons incident on Cu show that the ratio of the Fourier coefficients of the virtual inelastic potential to that of the crystal potential is in the order of 10^{-5}, which is less than experimental errors. Similar calculations for low-energy electrons are not available but this contribution will also be small. Although the small wave vector in the denominator of Yoshioka's expression increases the contribution of virtual inelastic scattering at low energies, this effect is more than compensated by the reduced probability of excitation when the beam energy becomes comparable with the ionization threshold.

The contribution of virtual inelastic phonon and plasmon scattering to the mean inner potential V_0 cannot be ignored. Ichikawa & Ohtsuki (1968) give a general method for estimating the effect using second-order perturbation theory. They estimate the phonon and plasmon corrections to the mean inner potential for a 250 V beam electron to be about 3 eV for Al. This value differs considerably from the value of 13.6 eV given by Pendry (1974) because of the different ways in which the potential was divided up. Pendry's value refers to an optical potential that excludes the ion-core contribution but includes contributions from exchange, virtual inelastic scattering and elastic scattering.

In summary, the most important corrections to the total optical potential are those arising from exchange and virtual inelastic scattering, which affect V_0, the contribution to V_g' due to absorption from phonon scattering and the contribution to V_0' due to inelastic scattering.

4. Computational results

Many-beam dynamical calculations have been completed based on (17) and (23) for thin Au films under plane-wave illumination with energies of 100–1000 eV. Absorption, virtual inelastic scattering and exchange corrections were all included in the manner described above. Exchange corrections to V_0 were included, but the small exchange corrections to V_g were ignored. Table 1 shows typical values of potential coefficients and corrections from various sources. Fig. 2 gives the total transmitted electron-beam intensity for 250 eV incident electrons. The value of the mean absorption used (5.7 V) resulted in an electron mean free path of about 9 Å, in agreement with estimates from LEED for Cu (Pendry, 1974). With a high-gain channel plate as detector, it is seen that transmission might be detected for thicknesses up to several nm for metals, as occurs around the edges of holes in transmission-electron microscopy samples or through small biological molecules.

To test the convergence of the Bloch-wave method used, a sequence of calculations were made with different numbers of beams included. Figs. 3(*a*)–(*c*) show that it was necessary to include about 50 beams in the calculations in order that the addition of more beams had negligible effect. Double-precision arithmetic was essential. The incorrect results given by the few-beam calculations indicate the importance of backscattering and multiple-scattering effects for low-energy electrons. To describe the electron-scattering process accurately and at the same time minimize the number of beams in the calculations, it was necessary to select with care the beams to be included in the calculations, with proximity to the Ewald sphere being the most important guide (Fig. 1*c*). For n beams, the computing time is proportional to n^2.

Owing to the small size of the Ewald sphere and the limited angular coherence of the field-emission tip, the Fourier images reported by Fink *et al.* (1991) are dominated by the interference between overlapping 111 and 000 orders (Spence & Qian, 1992). Fig. 4(*a*) shows the thickness dependence of these beams for 260 eV electrons, incident on a (110) Au film,

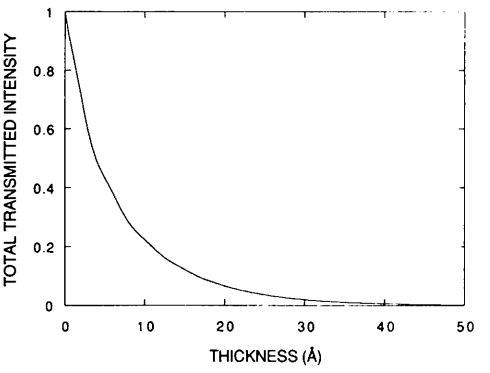

Fig. 2. The total transmitted intensity *versus* specimen thickness for normal incidence on Au(110). The incident electron energy is 250 eV. The zero-order absorption coefficient used gives a mean free path of about 9 Å.

travelling along [110]. Here, $n = 58$ beams have been included in the calculation. Region A ($t < 1$ Å) indicates the thickness region within which the zero-order intensity $I(000)$ is much larger than the 111 intensity, so that the single-scattering approximation holds and in-line electron holography allows (in principle) the reconstruction of the scattering potential (*i.e.* 'object reconstruction'). (In this approximation, as shown in Fig. 4 by the parabolic curve, the intensity is proportional to t^2). In region B, $I(000) > I(111)$ also, but reconstruction recovers the multiply scattered wavefield leaving the crystal ('image reconstruction'). Figs. 4(*b*)–(*e*) show similar results for other accelerating voltages. The effect of atomic number is indicated in Fig. 4(*f*), which shows calculations for Al at 260 V. The range of thickness within which the single-scattering approximation holds is seen to increase with increasing voltage and decreasing atomic number. Fig. 5 gives the variation of the same transmitted intensities with respect to incident-beam energy. A crystal thickness of 15 Å was used. Both the 000 and 111 beam intensities are highly sensitive to the incident electron energy due to the small size of the Ewald sphere. Each point on Fig. 5 required about 4 h of computing time on our VAX 3200 computer.

Fig. 6 shows the reflected-beam intensities for 250 eV electrons on Au (110) at normal incidence. For thicknesses greater than about 30 Å, the reflected-beam intensities approach a constant. Thus our method may also be used to calculate LEED intensities reflected from bulk crystals. In the point-source microscope, these beams are reflected back onto the surface by the intense tip field, where they hop along the surface, making detection difficult.

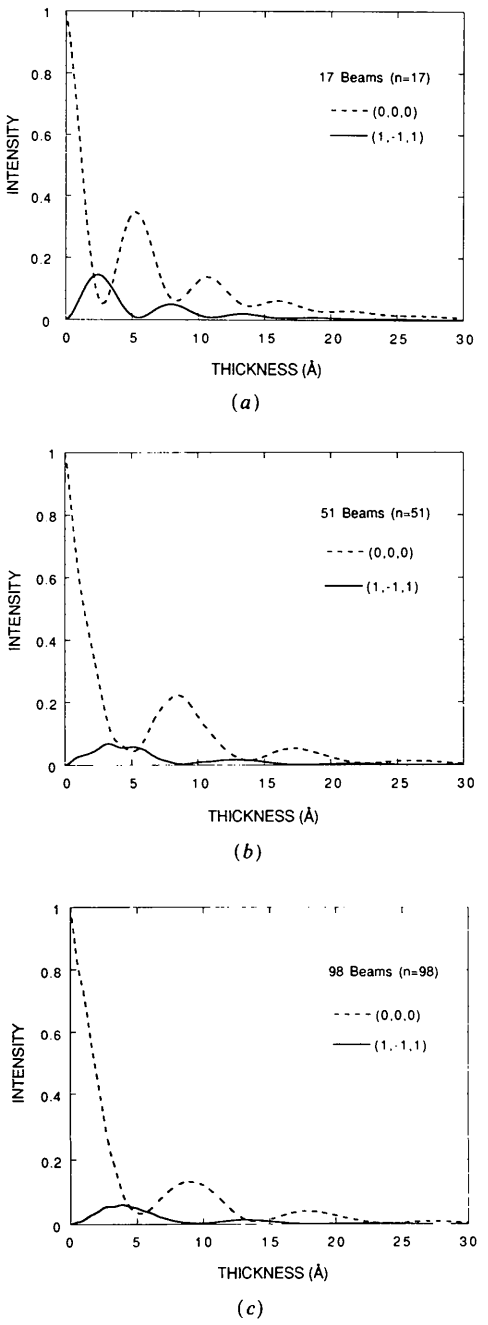

Fig. 3. A series of results used to test the convergence of the Bloch-wave calculations, for (*a*) 17, (*b*) 51 and (*c*) 98 beams. Little change is seen beyond the addition of about 50 beams but double precision arithmetic is essential. The incident electron energy is 250 eV, for normal incidence on Au(110).

5. Discussion and concluding remarks

For compact objects in the point-projection microscope that are smaller than the coherence width of the beam, the wavefield passing around the object may be used to provide the reference beam required for holography (Haine & Mulvey, 1952; Fink & Kreuzer, 1991). Thus, an image may be reconstructed holographically provided that the twin-image problem of the in-line geometry can be solved [*e.g.* by the method of lenseless Fraunhofer holography used to study aerosols (Thompson, Ward & Zinky, 1967)]. For this case of a finite object, our computational method may also be applied by constructing an artificial superlattice, containing, in one unit cell, the object and surrounding vaccum (Spence, 1978). It may readily be shown (Spence, 1992) that such a point-projection shadow image is identical (except for magnification) with the image that would be formed by use of plane-wave illumination on a plane distance z_1 downstream from the object. This result holds for weakly scattering laterally extended objects or for compact opaque objects. The focusing error z_1 cannot be removed by additional lenses but may be removed by holographic reconstruction for small objects.

We now consider the relationship between Fourier images and holography for laterally infinite semi-transparent periodic objects with a square lattice. In-line holography is impossible with such an exten-

ded object because of the twin-image problem. But Fourier images will be formed by interference between rays leaving the tip at angles differing by multiples of the Bragg angle, after diffraction through the crystal. Fig. 1(*a*) defines the wavefunction across the exit face of the crystal, $\Psi(1)$, and the wavefunction detected, $\Psi(2)$. According to Fourier-imaging theory (Cowley & Moodie, 1960), for a true point source, magnified copies $\Psi_n(2)$ of $\Psi(1)$ are formed on planes satisfying

$$1/z_1 + 1/z_2 = \lambda/2na^2, \tag{28}$$

where n is an integer and a the lattice constant. Aberration-free lensless imaging then occurs with magnification $M = z_2/z_1$. If the restriction is made to single-scattering conditions [region A on Fig. 4(*a*)]

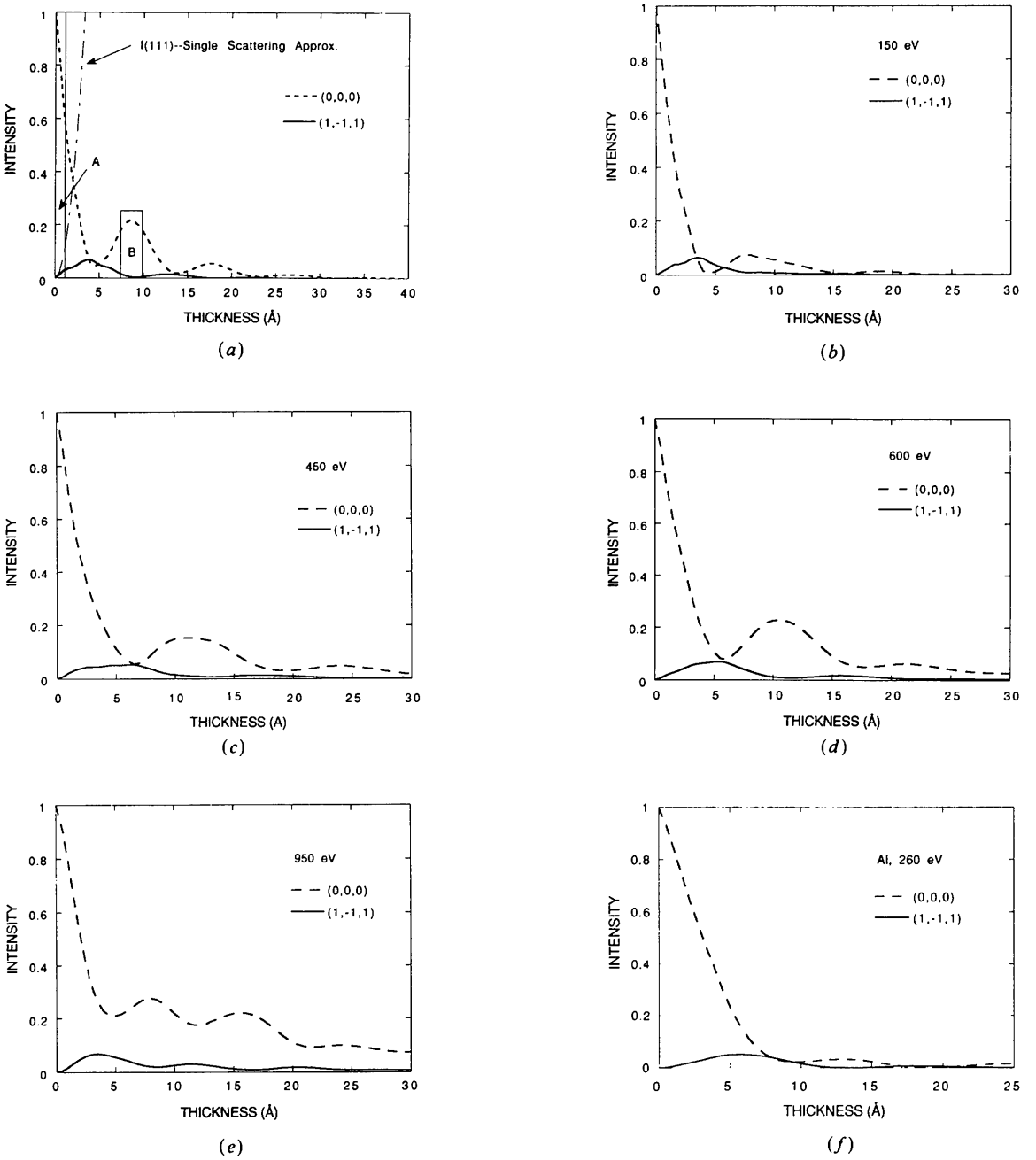

Fig. 4. The intensity of the 000 and 111 transmitted beams for (*a*) 260, (*b*) 150, (*c*) 450, (*d*) 600 and (*e*) 950 eV electrons incident on Au(110). (*f*) Intensity for 260 eV electrons on Al(110). 58 beams were included in the calculations. Region A ($t < 1$ Å) is the region of single scattering allowing holographic reconstruction of the crystal potential, while region B allows reconstruction of the multiple-scattering wavefunction leaving the crystal.

with resolution limited to the region in which the Ewald sphere is 'flat', then

$$\Psi(1) \simeq 1 - i\sigma V_p(\mathbf{r}), \tag{29}$$

where σ is an interaction constant and $V_p(\mathbf{r})$ is the two-dimensional optical potential $V_{\text{eff}}(\mathbf{r})$ projected in the beam direction. Then, apart from unimportant phase factors, the recorded Fourier image is $I(2) = \Psi(2)\Psi(2)^* = \Psi(1)\Psi(1)^*$ (for unit magnification) and so is proportional to $[V_p(r)]^2$. But the same intensity distribution $I(2)$ may be interpreted as a hologram if

$$\Psi(2) \simeq 1 + \varepsilon, \tag{30}$$

where ε is small and complex. Equation (29) (single scattering) is a sufficient condition for (30) (holography) and

$$I(2) \simeq 1 + \varepsilon + \varepsilon^*. \tag{31}$$

If a reconstruction of this hologram is attempted, the resulting real and virtual images can only be separated in the in-line geometry if the object is small (Thompson, Ward & Zinky, 1967), in which case it is possible to reconstruct $V_p(\mathbf{r})$ rather than its square (as for Fourier images). The case of Fourier images occurring at edges has recently been treated by Clauser & Reinsch (1992).

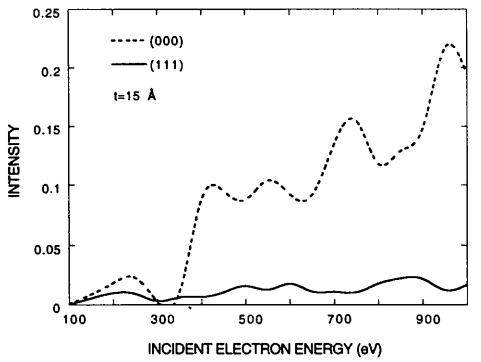

Fig. 5. The variation of transmitted intensity with incident-beam energy for Au(110). The crystal thickness is 15 Å.

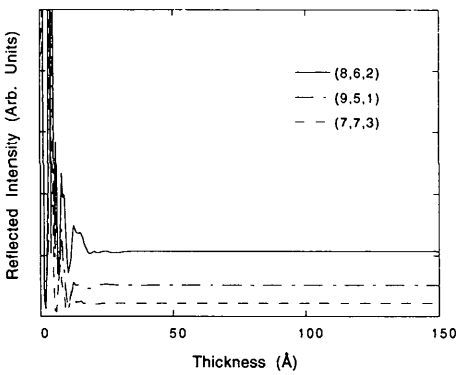

Fig. 6. The reflected-beam intensities for 250 eV incident electrons on Au(110) at normal incidence. The constant intensity at large thickness indicates that this method can be used to calculate reflected intensities from bulk crystals.

For finite molecules whose thickness exceeds a few atomic layers, the quantity that might be recoved by in-line holography (if the twin-image problem can be solved) is the multiply scattered wavefunction $\Psi(1)$ (the 'image'), not the optical potential $V_{\text{eff}}(\mathbf{r})$ (the 'object'). $\Psi(1)$ may have either maxima or minima at atomic sites but preserves the symmetry of $V_p(\mathbf{r})$. The resolution is given by the effective source size. The recovery of the optical-scattering potential $V_{\text{eff}}(\mathbf{r})$ from $\Psi(1)$ requires a unique solution to the inversion problem of quantum mechanics. By comparison with early attempts at point-projection electron holography (Haine & Mulvey, 1952), the low-voltage instruments using physical sources have greatly reduced aberration coefficients in the sub-nanometer range (Scheinfein, Qian & Spence, 1992).

The 'object' one wishes to view with a TLEED microscope might alternatively be defined as the ground-state crystal charge density. This is recoverable (using Poisson's equation) from the optical potential $V_{\text{eff}}(\mathbf{r})$ only if the exchange and virtual-scattering corrections are negligible. This occurs at high energies. Since the largest corrections are for $V(000)$, these corrections will appear as an artificial enhancement of the outer bonding-electron density (Becker & Coppens, 1990; Spence & Zuo, 1992). For an object whose transmission function is a phase grating, source and detctor positions can be found such that the Fourier images directly resemble the projected charge density in the crystal (Cowley & Moodie, 1960). Fig. 1(*c*) shows that this is a very poor approximation at LEED energies.

Since only a single set of equivalent beams is scattered in the forward direction for gold, the periodicity of Fourier images with axial-tip coordinate will not be observed, since the 'object' is sinusoidal. A sinusoidal object is always in focus (Rayleigh, 1881).

The question arises as to the best choice of accelerating voltage for atomic-resolution imaging. This involves a compromise between many competing factors. Two of the most important concern image interpretation and radiation damage [see Buseck, Cowley & Eyring (1989) for a review]. At high voltages (hundreds of kV), the single-scattering approximation becomes accurate for conveniently large sample thicknesses, greatly simplifying image interpretation. An intuitive image interpretation becomes possible within the point resolution of the instrument (currently about 1.5 Å at 400 kV). Although ionization damage also decreases with accelerating voltage according to the Bethe law, displacement damage increases with accelerating voltage and machines become very expensive. As the voltage approaches the ionization threshold, the Bethe stopping-power law fails and detailed calculations are required for each material [Inokuti (1971) and references therein].

At low voltages, ionization damage may become severe, resulting in atomic displacement through the radiolysis process (Hobbs, 1983), but displacement damage does not occur. However, multiple scattering greatly complicates image interpretation at low energies, as indicated by these calculations. (For example, it is difficult to determine whether atoms appear white or black.) Thus, interpretability is maximized and damage minimized by working at a voltage just below the knock-on threshold for surface atoms or defects. For the point-source microscope shown in Fig. 1(*a*), for a given tip radius, the maximum voltage is limited by field desorption and this voltage and the magnification are not independent since both depend on z_1. The use of an accelerator introduces aberrations or, if micrometer-sized lenses are used, alignment difficulties. Other factors influencing the choice of accelerating voltage include the increase of source brightness with voltage and the decrease in detector efficiency with voltage (commensurate with weaker sample interaction). Higher-speed recording with efficient detectors reduces the effects of radiation damage. If magnetic electron lenses are used, the reduction in wavelength at higher voltage more than compensates for increased lens aberrations but electronic (incoherent) instabilities in power supplies must be considered (Spence, 1988). Aberration coefficients for the virtual source used by Fink *et al.* (1991) are extremely small because of the small radius of curvature of the tip field (Scheinfein, Qian & Spence, 1992). In summary, interpretability [in terms of $V(r)$, not $V_{\text{eff}}(r)$], source brightness, ionization-damage conditions and lens performance all improve with increasing accelerating voltage, whereas ballistic damage increases and detector efficiency decreases. The best all-round compromise would appear to consist of a field-emission point-projection instrument operating just below the knock-on threshold, if such an instrument could be built and aligned, using micrometer-sized electrostatic-lens apertures to form the source at about 200 kV.

The most important results from this work concern the validity domain of the single-scattering approximation (summarized in Fig. 4). We find that this approximation fails for monolayer thicknesses of heavy- and light-element crystals at energies below 1 kV and similar results can be expected for organic molecules. Single-scattering conditions can sometimes be identified experimentally since they result in a weak image modulation on a strong background, but this may be confused with regions such as *B* on Fig. 4(*a*).

This work was supported by NSF grant no. DMR91-12550. We are grateful to Dr M. Scheinfein for many useful discussions.

References

BECKER, P. & COPPENS, P. (1990). *Acta Cryst.* A**46**, 254–258.
BETHE, H. A. (1928). *Ann. Phys. (Leipzig)*, **87**, 55–129.
BIRD, D. & KING, Q. A. (1990). *Acta Cryst.* A**46**, 202–208.
BLACKMAN, M. (1939). *Proc. R. Soc. London Ser. A*, **173**, 68–82.
BOERSCH, H. (1942). *Naturwissenschaften*, **30**, 120–123.
BUSECK, P., COWLEY, J. M. & EYRING, L. (1989). *High-Resolution Transmission Electron Microscopy.* Oxford Univ. Press.
CLAUSER, J. F. & REINSCH, M. (1992). *Appl. Opt.* In the press.
COLELLA, R. (1972). *Acta Cryst.* A**28**, 11–15.
COWLEY, J. M. (1981). *Ultramicroscopy*, **7**, 19–26.
COWLEY, J. M. & MOODIE, A. F. (1960). *Proc. Phys. Soc. London Sect. B*, **76**, 378–384.
FINK, H. W. & KREUZER, J. (1991). *Sci. News*, **140**, 186.
FINK, H. W., SCHMID, H., KREUZER, H. J. & WIERZBICKI, A. (1991). *Phys. Rev. Lett.* **67**, 1543–1546.
HAINE, M. E. & MULVEY, T. (1952). *J. Opt. Soc. Am.* **42**, 763–773.
HALL, C. R. & HIRSCH, P. B. (1965). *Proc. R. Soc. London Ser. A*, **286**, 158–177.
HIRSCH, P., HOWIE, A., NICHOLSON, R. B., PASHLEY, D. W. & WHELAN, M. J. (1977). *Electron Microscopy of Thin Crystals.* Florida: Kreiger.
HOBBS, L. (1983). *Quantitative Electron Microscopy. Proc. of the 25th Scottish Universities Summer School in Physics, NATO Advanced Study Institute*, edited by J. CHAPMAN & A. CRAVEN, pp. 399–445. Scottish Universities Summer School in Physics, Glasgow.
HUMPHREYS, C. J. (1979). *Rep. Prog. Phys.* **42**, 1826–1886.
ICHIKAWA, M. & OHTSUKI, Y. H. (1968). *J. Phys. Soc. Jpn*, **27**, 953–956.
INOKUTI, M. (1971). *Rev. Mod. Phys.* **43**, 297–343.
International Tables for Crystallography (1992). Vol. C. Dordrecht: Kluwer Academic Publishers.
JONES, E. R., MCKINNEY, J. T. & WEBB, M. B. (1966). *Phys. Rev.* **151**, 476–483.
KAMBE, K. (1988). *Acta Cryst.* A**44**, 885–890.
LUNDQVIST, B. I. (1969). *Phys. Status Solidi*, **32**, 273–280.
MAKSYM, P. A. (1988). In *RHEED and REM*, edited by P. LARSEN & P. DOBSON. New York: Plenum.
METHERELL, A. J. F. (1975). *Electron Microscopy and Materials Science. Third Course of the International School of Electron Microscope*, edited by U. VALDRE & E. REUDL, pp. 397–552. Commission of the European Communities, Directorate General, Scientific and Technical Information, Brussels.
PENDRY, J. B. (1974). *Low Energy Electron Diffraction.* New York: Academic Press.
RADI, G. (1970). *Acta Cryst.* A**26**, 41–56.
RAYLEIGH, LORD (1881). *Philos. Mag.* **11**, 196–203.
REZ, P. (1978). *Acta Cryst.* A**34**, 48–51.
SCHEINFEIN, M., QIAN, W. & SPENCE, J. C. H. (1992). *J. Appl. Phys.* In the press.
SLATER, J. C. (1951). *Phys. Rev.* **81**, 385–390.
SLATER, J. C. (1967). *Insulators, Semiconductors and Metals.* New York: McGraw-Hill.
SPENCE, J. C. H. (1978). *Acta Cryst.* A**34**, 112–116.
SPENCE, J. C. H. (1988). *Experimental High Resolution Electron Microscopy*, 2nd ed. Oxford Univ. Press.
SPENCE, J. C. H. (1992). *Optik (Stuttgart)*. In the press.
SPENCE, J. C. H. & QIAN, W. (1992). *Phys. Rev. B*, **45**, 10271–10279.
SPENCE, J. C. H. & ZUO, J. M. (1992). *Electron Microdiffraction.* New York: Plenum.
STERN, R. M., PERRY, J. J. & BOUDREAUX, D. S. (1969). *Rev. Mod. Phys.* **41**, 275–295.
THOMPSON, B. J., WARD, J. H. & ZINKY, W. (1967). *Appl. Opt.* **6**, 519–526.
TONOMURA, A. (1987). *Rev. Mod. Phys.* **59**, 639–669.
YOSHIOKA, H. (1957). *J. Phys. Soc. Jpn*, **12**, 618–628.
ZHAO, T. C. & TONG, S. Y. (1988). *Ultramicroscopy*, **26**, 151–159.